ACS OMEGA

http://pubs.acs.org/journal/acsodf

Article

Insights into the pH-Dependent Adsorption Behavior of Ionic Dyes on Phosphoric Acid-Activated Biochar

Fang Wei, Yuwei Zhu, Tongmin He, Shengpu Zhu, Tianhao Wang, Chunyi Yao, Chenlu Yu, Peipei Huang, Yan Li, Qiang Zhao,* and Weiguo Song

Cite This: *ACS Omega* 2022, 7, 46288−46302

Read Online

ACCESS | Metrics & More | Article Recommendations | Supporting Information

ABSTRACT: Activated biochar is a promising porous carbonaceous adsorbent material for organic pollutant removal, but it remains challenging to obtain high porosity and aromaticity through a simple and low-cost synthetic method. The common adsorption mechanisms of organic dyes on activated biochar should be further investigated in order to guide the synthesis of high-efficiency adsorbent materials. Here, we proposed a high-yield (up to 40 wt %) synthetic method of phosphoric acid-activated biochar from pomelo peel (PPC) with a high specific area of 877.3 m^2/g through a facile thermal treatment at a relatively low temperature (250 °C). The specific activation mechanism of H_3PO_4 in the preparation of the adsorbent was investigated by a range of experiments and characterizations. The kinetic and isotherm experiments are also conducted to evaluate its dye adsorption behavior. According to the adsorption experiment results, PPC exhibits high saturated adsorption capacities for methyl orange (MO, 239.1 mg/g), rhodamine B (RhB, 2821.8 mg/g), methylene blue (MB, 580.5 mg/g), and crystal violate (CV, 396.6 mg/g) according to the Langmuir model. The maximum initial concentration of each dye solution for acquiring 90% removal efficiency is estimated to be 234.55 ppm (MO), 2943.8 ppm (RhB), 633.8 ppm (MB), and 423.6 ppm (CV) at 298 K with an adsorbent dosage of 1 g/L. The characterization results also indicate PPC has a complex synergetic mechanism for ionic dye adsorption behavior. This provides perspectives regarding PPC as a promising biochar adsorbent from biomass waste, which is probably useful for high-efficiency dye removal in water treatment.

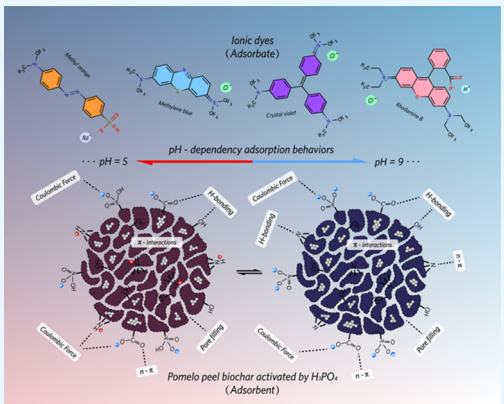

1. INTRODUCTION

Nowadays, much progress has been made in industrial and agricultural development, which also brings water pollution caused by organic pollutants, heavy metal ions, fertilizers, pesticides, and antibiotic drugs, posing a serious hazard to aquatic living organisms and even humanity.[1] Water pollution due to discharged dye effluents from the textile industry is one of the major threats to the ecological system. Because of their color problem, high chemical oxygen degree (COD), non-biodegradability, carcinogenicity, toxicity, and mutagenicity, organic dyes are hazardous materials that should be fully removed from textile effluents.[2−4] Many efforts have been made into the investigation of high-efficiency water treatment techniques, such as advanced oxidation processes (AOPs),[5] chemical reduction processes (CRPs),[6] photocatalytic methods (PCMs),[7] electrocatalytic methods (ECMs),[8] membrane separation processes (MSPs),[9] adsorption,[10−13] biodegradation,[14] etc. Unfortunately, several disadvantages, like high cost, high energy consumption, toxic sludge or byproduct formation, and limited degradation efficiency, have hindered their large-scale application.

Though there exists a potential risk of the toxicity of effluents due to residual adsorbents or byproducts, adsorption is one of the most widely used methods for soluble pollutant removal from wastewater due to its low-cost advantage, wide compatibility, and ease of operation.[15] Porous carbonaceous materials are considered to be environmentally friendly and nontoxic adsorbents in practical use. To be specific, activated carbons (ACs) derived from fossil-based feedstocks have been widely applied for the efficient adsorption of water pollutants in the past few decades.[16] Generally, ACs are subjected to a high temperature (400−600 °C) in specific conditions (non-circulated air atmosphere, inert atmosphere, vacuum), which is usually followed by activation with chemicals (e.g., CO_2, H_2O steam, acid, base, and salts) at a higher temperature (above 800 °C).[17] High aromaticity and porosity with a large specific

Received: July 29, 2022
Accepted: November 16, 2022
Published: December 7, 2022

surface area in ACs are essential factors for the favorable adsorption of organic contaminants in an aqueous solution. However, several disadvantages, like nonrenewable feedstocks, complicated synthesis methods, high energy consumption, and low yield, are non-negligible in the field of producing commercial ACs. The growing demand for low-cost and high-efficiency alternative carbonaceous adsorbents like biochar which is synthesized from biowaste feedstocks is currently urgent.

Biochar is a solid material derived from the carbonization of biomass. Biomass such as fruit peels and plant roots can be converted into biochar,[18,19] which avoids large amounts of greenhouse CO_2 emissions from conventional decaying and incineration.[20] Biochar has also been developed for the purpose of carbon sequestration, water holding, and nutrient storage. But restrained by limited porosity, biochar is not yet such an effective adsorbent as AC. To overcome these drawbacks, activated biochar with enhanced porosity and higher specific surface area through chemical activation and pyrolysis at relatively low temperature (<350 °C) in a non-circulated air atmosphere has become a kind of attractive adsorbent material, especially for adsorption of organic dyes, phenols, pesticides, and heavy metal ions.

Pomelo peel (almost 40% of total pomelo weight) is usually treated as agricultural waste, which is abundant in pectin, hemicellulose, cellulose, and lignin. Benefiting from its complex soft network structures, pomelo peel has been modified as a potential carbonaceous adsorbent material. Ren et al. prepared an anionic adsorbent via citrate-grafted pomelo peel with a moderate thermal treatment (120 °C), which enhanced the adsorption of methylene blue via surface modification when compared with pomelo peel.[21] Zhao et al. have reported a low-temperature (250 °C) one-step synthesis of phosphoric acid-activated biochar derived from pomelo peel, which exhibited good adsorption for heavy metal ions due to a strong chemical adsorption mechanism.[22] Zhang et al. synthesized phosphoric acid-activated biochar from pomelo peel wastes at a higher thermal treatment temperature (450 °C) and investigated its adsorption behavior for methyl orange dye removal.[23] Wu et al. confirmed that the phosphoric acid-activated pomelo peel takes the electrostatic interaction accompanied by ion exchange as the main adsorption mechanism for hexavalent chromium removal.[24] However, very few studies have revealed the detailed activation effect of phosphoric acid during thermal treatment in the preparation of biochar, which is of importance to understanding the critical changes of structure and surface chemistry in the synthesis of those adsorbents. What was also neglected is that different types of ionic dye have potential variations in their molecular structures at different pH, which is also sensitive to the adsorption mechanism. In this case, the intermolecular forces between adsorbent and adsorbate are needed to be further investigated in order to propose the mechanism for ionic dye adsorption on biochar.

In this article, pomelo peel biochar (PPC) was synthesized through phosphoric acid activation and low-temperature pyrolysis, which is used for ionic dye removal. The structural morphology, pore structure, pore size distribution, surface functional groups, aromaticity, and surface charge polarity were investigated. The phosphoric acid activation mechanism was revealed via in situ thermal analysis and the corresponding characterization results. Functional group characterization was fully investigated to determine the possible active sites for ionic dye adsorption on PPC. The common kinetic models (the pseudo-first-order kinetic model, the pseudo-second-order kinetic model, and the intraparticle diffusion model) and isotherm models (the Langmuir isotherm model, the Freundlich isotherm model, and the Redlich−Peterson isotherm model) were used to fit the experimental data to evaluate the adsorption performance. The effects of initial pH on anionic, cationic, and neutral dye adsorption on PPC were investigated. The probable adsorption mechanisms were discussed based on the above results.

2. MATERIALS AND METHODS

2.1. Materials. Methyl orange (MO, Mw = 327.34 g/mol), rhodamine B (RhB, Mw = 479.02 g/mol), methylene blue (MB, Mw = 373.9 g/mol), and crystal violet (CV, Mw = 407.99 g/mol) were purchased from Beijing Innochem Science & Technology Co., Ltd. and Sinopharm Chemical Reagent Co., Ltd. Phosphoric acid (H_3PO_4, analytically pure (AR), ∼85%) and sodium hydrate (NaOH, AR, ∼99%) were purchased from local chemical reagent companies in Tianjin. Pomelos were purchased from a local market. All the chemicals were used directly without any further purification, and the dye stock solutions were prepared by dissolving accurately weighed dye in distilled water. The experimental solution was obtained by diluting the dye stock solution in accurate proportions to different initial concentrations.

2.2. Preparation of PP. The pomelo peel was sliced into small pieces and washed with deionized water twice prior to being dried in an air oven at 50 °C for 48 h. These dry pomelo peel pieces were then crushed into powder. Finally, PP powder was filtered through a 60-mesh stainless steel sieve and collected for further use.

2.3. Preparation of PPC. A 2.0 g sample of PP was uniformly impregnated in 5.0 g of H_3PO_4 (85 wt %) for 24 h, which is obtained as a PP-250 precursor. Then, it was transferred into a 40 mL ceramic crucible for pyrolysis at 250 °C for 1 h in a muffle furnace with a heating rate of 5 °C/min. The sample was naturally cooled to nearly 50 °C and then transferred into an agate mortar for grinding until there was no macroscopic block adhesion. The obtained intermediate product was denoted as PP-250. 100 mL of NaOH (0.1 mol/L) solution was mixed with PP-250, which was stirred for 1 h. Subsequently, the liquid−solid mixture was filtrated and rinsed with deionized water for neutrality. Around 0.8 g of PPC was eventually obtained by forced air drying at 50 °C for 24 h. The schematic diagram of the PPC preparation method is shown in Figure S1.

2.4. Characterization. The surface morphology of PP and PPC was analyzed by scanning electron microscopy (SEM, JEOL-6701). The specific surface area and the pore structure analysis were measured by using the JW-BK200C BET analyzer via the N_2 adsorption−desorption method. Thermogravimetric analysis (TGA) was performed on an SDT-Q600 instrument at a heating rate of 5 °C min^{-1} in air. The Fourier transform infrared (FT-IR) spectra were recorded in the 4000−400 cm^{-1} region by a Nicolet IS10 instrument. The X-ray photoelectron spectroscopy (XPS) was measured on a Thermo ESCALAB 250xi. The Raman spectra were obtained by a DXR3 microlaser Raman spectrometer with a laser wavelength of 532 nm. The surface zeta potential of PPC particles dispersed in an aqueous solution at different pH (3, 5, 7, 9, and 11) was analyzed by using a laser particle analyzer (Zetasizer Nano ZS90). The concentrations of dye in solutions were determined by the spectrophotometry method on an

https://doi.org/10.1021/acsomega.2c04799
ACS Omega 2022, 7, 46288−46302

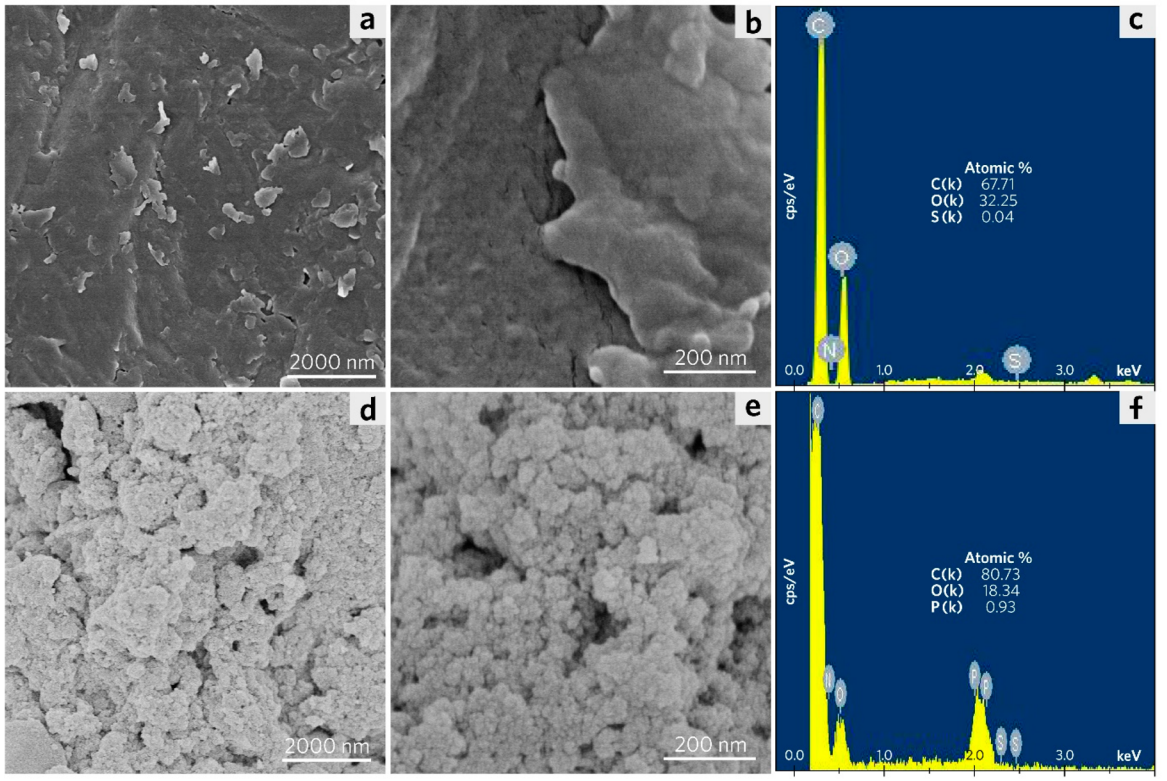

Figure 1. SEM images of PP (a and b) and PPC (d and e); (c) EDS pattern of PP and its atomic ratio of C, O, and S; (f) EDS pattern of PPC and its atomic ratio of C, O, and P.

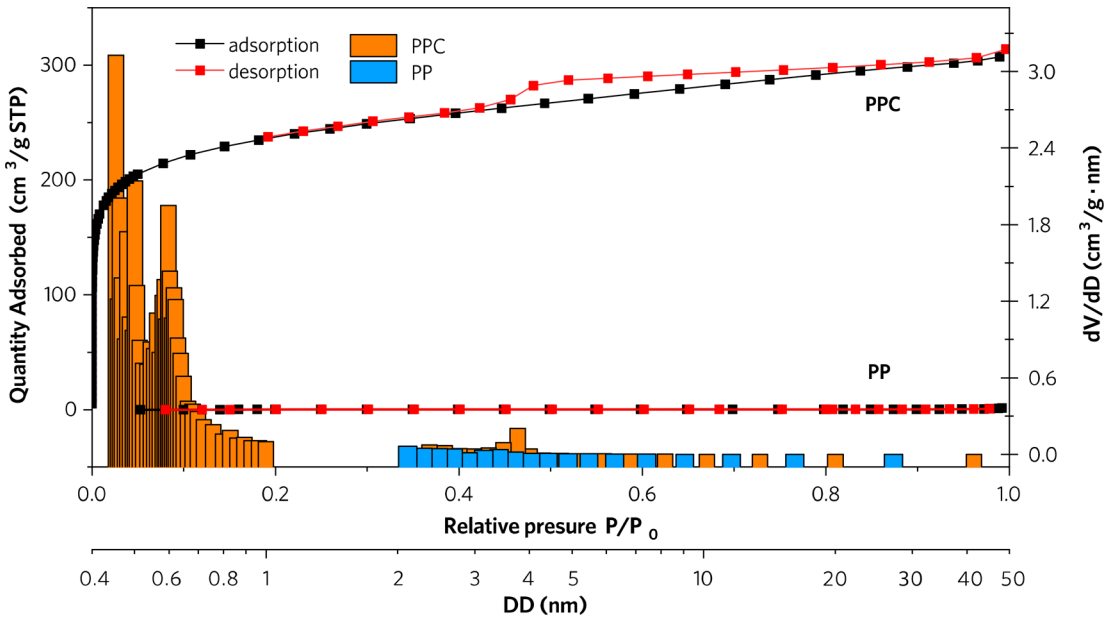

Figure 2. N_2 adsorption−desorption isotherms and pore size distribution bar charts of PP and PPC.

N5000 Plus UV−vis spectrometer at a specific wavelength (MO, 465 nm; RhB, 555 nm; MB, 246 nm; CV, 302 nm).

2.5. Adsorption Experiments. Adsorption experiments were conducted in a set of 50 mL centrifuge tubes containing 20 mg of PPC adsorbent and 20 mL of dye solutions with different initial concentrations (50, 100, 200, 250, and 300 ppm for MO; 1000, 2000, 3000, and 4000 ppm for RhB; 200, 500, 800, and 1000 ppm for MB; 50, 100, 200, 300, 400, and 500 ppm for CV). The centrifuge tubes were vibrated in an air bath shaker at 120 rpm and 25 °C until equilibrium adsorption was accomplished. The adsorption isotherms were plotted by equilibrium dye concentration (c_e, which was determined by the UV−vis absorbance value at 470 nm for MO, 554 nm for RhB, 246 nm for MB, and 302 nm for CV on the basis of their standard curves) in liquid phase versus equilibrium adsorption capacity of dye in solid phase (q_e, which was calculated from the mass balance equation as below).

https://doi.org/10.1021/acsomega.2c04799
ACS Omega 2022, 7, 46288−46302

Table 1. Textural and Structural Parameters of PP and PPC

sample name	S_{BET}(m^2/g)	S_{meso}(m^2/g)	V_{total}(cm^3/g)	V_{micro}(cm^3/g)	V_{meso}(cm^3/g)	most probable D_{micro} (nm)	most probable D_{meso} (nm)
PP	0.5503	0.4454	0.00143		0.0005		
PPC	887.281	219.334	0.486	0.3434	0.212	0.4722	3.847

$$q_e = \frac{c_0 - c_e}{M} \cdot V$$

where c_0 and c_e are the initial and equilibrium dye concentrations (mg/L), respectively; q_e is the equilibrium adsorption capacity of dye (mg/g), while M and V are the weight of the adsorbent (g) and the volume of dye solution (L), respectively.

The adsorption kinetic experiments were conducted by varying the contact time (5, 10, 30, 60, 180, and 360 min) with initial dye concentrations of 200 mg/L for MO, 1000 mg/L for RhB, 300 mg/L for MB, and 300 mg/L for CV, with PPC dosage of 10 mg/20 mL at 25 °C. The adsorption capacity versus contact time at different temperatures was measured in order to investigate its adsorption kinetic process.

The pH-dependent adsorption experiments were conducted by varying initial pH from 3 to 11, with initial dye concentrations of 182 mg/L for MO, 1417 mg/L for RhB, 592 mg/L for MB, and 379 mg/L for CV, with a PPC dosage of 10 mg/20 mL at 25 °C. The different initial pH of the solution was adjusted by the addition of hydrochloric acid (0.6 mol/L) or sodium hydroxide solutions (0.6 mol/L) and was eventually identified by a pH meter. The influence of initial pH values on the UV−vis adsorption spectrum of each dye is presented in Figure S2.

3. RESULTS AND DISCUSSION

3.1. Morphology and Surface Characterization of PP and PPC. SEM images have shown the morphological characteristics of pomelo peel (PP) and pomelo peel chars (PPC). Figure 1a,b reveals that PP has a complex structured morphology with abundant smooth wrinkles. The energy-dispersive spectroscopy (EDS) analysis (Figure 1c) confirms very few S, abundant C, and O with a C/O atomic ratio of 2.10 for PP. In contrast, PPC shows a granular rough surface morphology with the pore structures shown in Figure 1d,e. According to Figure 1f, the characteristic spectrum line of P is presented in the EDS pattern of PPC, which indicates the P bonded to surface structures. In particular, the C/O atomic ratio of PPC rises to 4.40, which indicates the occurrence of dehydration and carbonization in the synthesis of PPC from PP.

The N_2 adsorption−desorption isotherms of PPC have shown a typical type I curve with an H4 hysteresis loop (Figure 2), whereas the BET surface area of PP is only 0.5503 m^2/g due to its loose and nonporous structure. The enhanced surface area of PPC is attributed to its abundant micropores and mesopores, which contribute to the high BET surface area of 877.3 m^2/g. The Barrett−Joyner−Halenda (BJH) and Horvath−Kawazoe (HK) methods are used to calculate the pore size distribution of PPC from the desorption branch. The most probable pore diameters of mesopores and micropores are 3.847 and 0.472 nm, respectively, as shown in Table 1. They provide evidence of morphology and surface changes from PP to PPC. The high porosity of PPC is proved to be induced by activation and pyrolysis.

3.2. Thermal Analysis of PP and PP-250 Precursor. To reveal the activation mechanism in the synthesis of PPC, the pyrolysis of PP and PP-250 precursor in the air atmosphere are conducted by *in situ* thermal analysis as shown in Figure 3.

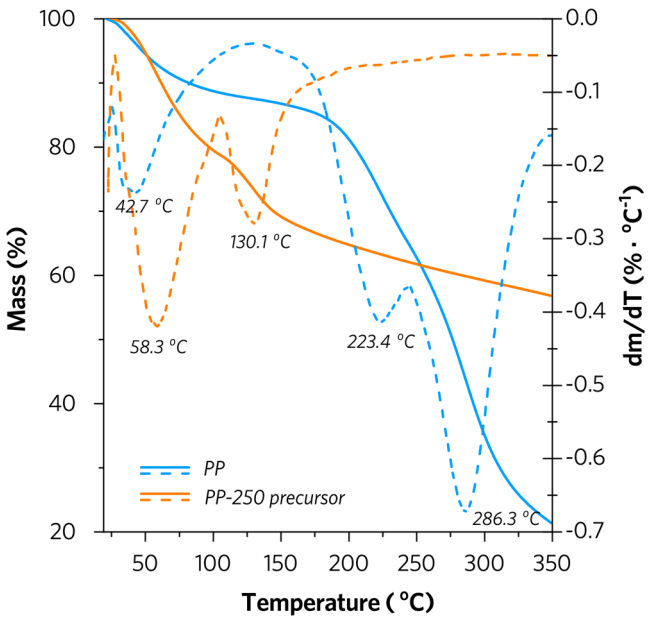

Figure 3. TGA curves (solid line) and DTG curves (dashed line) of PP and PP-250 precursor during the *in situ* pyrolysis process in the air at a heating rate of 5 °C/min.

Great changes in thermal mass loss procedures can be found between PP and PP-250 precursor. The maximum loss of adsorbed water happens at 42.7 °C for PP. Benefiting from the treatment of phosphoric acid, the mass loss temperature of adsorbed water in PP-250 precursor slightly increases to 58.3 °C. Subsequently, a significant mass loss procedure occurs in a temperature range from 104.7 to 350 °C for the PP-250 precursor, which is assigned to the formation of polyphosphoric acids and oxidative decomposition of hydrocarbons. Notably, the decomposition of PP begins at nearly 128.9 °C, in which process the pyrolysis of hemicellulose happens with a maximum mass loss rate of 0.413 wt %/°C at 223.4 °C prior to the pyrolysis of cellulose with a maximum mass loss rate of 0.672 wt %/°C at 286.3 °C. The decomposition of the PP-250 precursor has been suppressed over the whole temperature range, leading to a mass loss rate being less than 0.067 wt %/°C above 200 °C. After the loss of adsorbed water, the condensed phosphoric acid transforms into a mixture of phosphoric acids and polyphosphoric acids, including species like H_3PO_4, $H_4P_2O_7$, and $H_5P_3O_{10}$ in higher proportion and $H_{n+2}P_nO_{3n+1}$ ($n > 4$) in lower proportion.[25] In PP-250, the highly cross-linked structures are developed by phosphoric acid activation and thermal treatment. The limited decomposition of hemicellulose and cellulose contributes to the formation of the micropore and mesopore structures of PPC, also achieving a high production yield of up to 40% for synthesized PPC (dry weight) from pomelo peel.

https://doi.org/10.1021/acsomega.2c04799
ACS Omega 2022, 7, 46288−46302

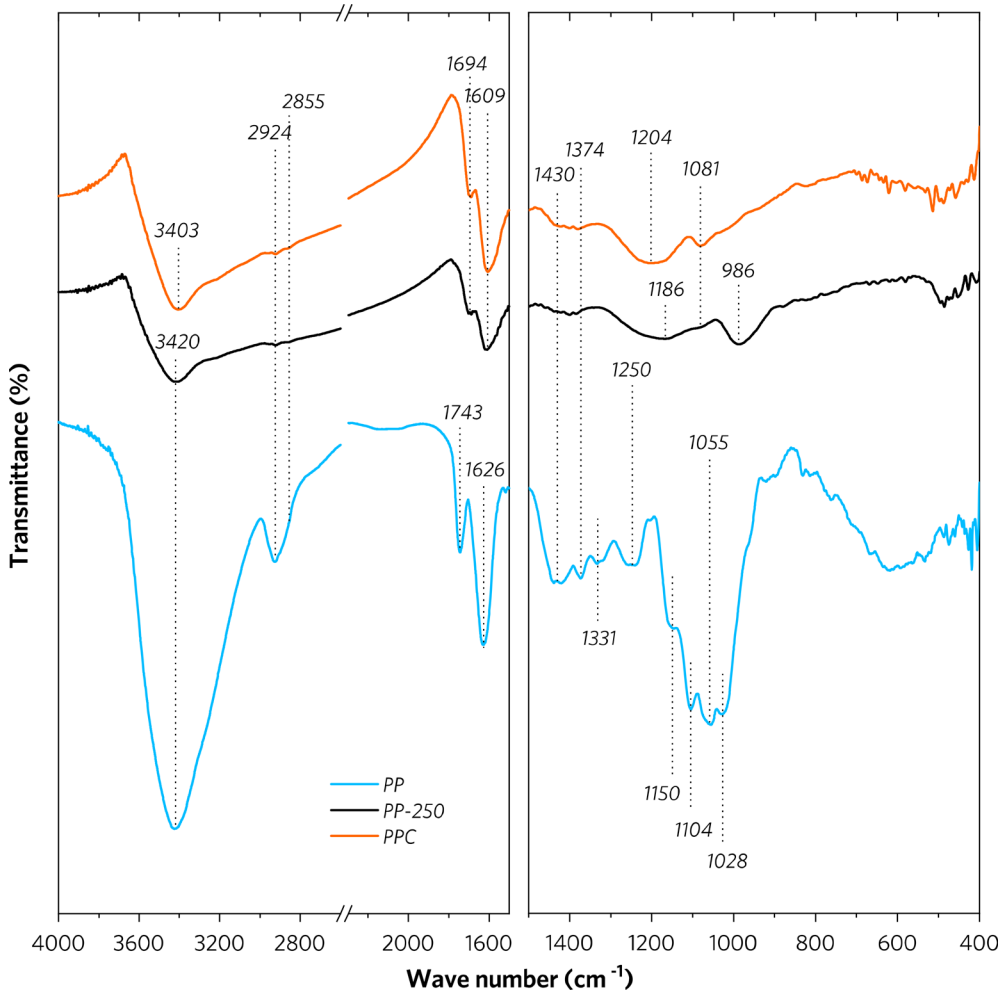

Figure 4. FTIR spectra of PP, PP-250, and PPC.

3.3. Functional Group Characterization of PP, PP-250, and PPC. The FT-IR spectra of PP, PP-250, and PPC are shown in Figure 4. The main functional groups of PP are depicted as follows: −OH, C−H, ester C=O, aromatic C=C, alcohol C−O, and ether C−O−C. The broad absorption band located around 3420 cm^{-1} is ascribed to the O−H stretching vibrations of hydroxyl groups and adsorbed water in PP and PP-250. Interestingly, for PPC, it shows a slight red shift to 3403 cm^{-1}, which indicates the increased interaction between hydroxyl groups. The absorption bands observed at 2924, 1430, and 1374 cm^{-1} can be attributed to C−H stretching and bending vibrations of methyl ($-CH_3$), methylene ($-CH_2-$), and methoxy groups ($-OCH_3$) in PP, PP-250, and PPC, respectively. There is an obvious redshift of the C=O stretching vibration band from 1743 to 1694 cm^{-1}, which indicates the loss of ester carbonyl groups ($-COOCH_3$) in pectin and the formation of aromatic carboxylic acid in the structure of lignin in PPC. The phosphate acid plays a crucial role in activating the hydrolysis of the ester. The band at 1626 cm^{-1} can be assigned to the C=C stretching vibration of the aromatic ring structure in PP (lignin). As for PP-250 and PPC, a similar red-shift happens from 1626 to 1609 cm^{-1}, which is attributed to the pyrolysis enhancing the degree of aromatic ring conjugation in PP-250 and PPC as compared with PP. Moreover, the band at 1331 cm^{-1} is evident for O−H bending vibrations of alcoholic hydroxyl groups. The bands at 1250 and 1150 cm^{-1} represent the C−O−C stretching vibrations of the aromatic ether of lignin and aliphatic ether of cellulose or hemicellulose, respectively. The bands at 1104 and 1055 cm^{-1} are assigned to the C−O bending mode of secondary and primary alcohol for cellulose and lignin.

In the FT-IR spectra of PP-250 and PPC, the broad absorption bands at 1168−1204 cm^{-1} are primarily attributed to the stretching modes of hydrogen-bonded P=O (PP-250) and free P=O (PPC). The O−C stretching vibrations in the P−O−C (aromatic) linkage or P(=O)OH bond is also attributed to these bands, which indicates the presence of phosphate esters in prepared samples.[26] The shoulder peak at 1081 cm^{-1} may be ascribed to the ionized linkage P^+-O^- in phosphate esters.[27] In the FTIR spectrum of PP-250, the absorption band at 986 cm^{-1} is probably due to P−O−C (aliphatic) stretching, P−O−C (aromatic) asymmetric stretching, and P−O−P asymmetric stretching in polyphosphates.[28] As a result, this band significantly decreases in the FTIR spectrum of PPC, which is attributed to the hydrolysis of phosphate esters and decomposition of polyphosphate when PPC is synthesized from PP-250 through pyrolysis.

To further identify the chemical structure change from PP to PPC, the XPS analysis was performed (Figure 5). According to the wide-scan XPS spectra, as shown in Figure 5a,b, both PP and PPC have the C-1s, N-1s, O-1s K 3p, and Ca 3p peaks but extra P-2s and P-2p peaks are observed only in the XPS

https://doi.org/10.1021/acsomega.2c04799
ACS Omega 2022, 7, 46288−46302

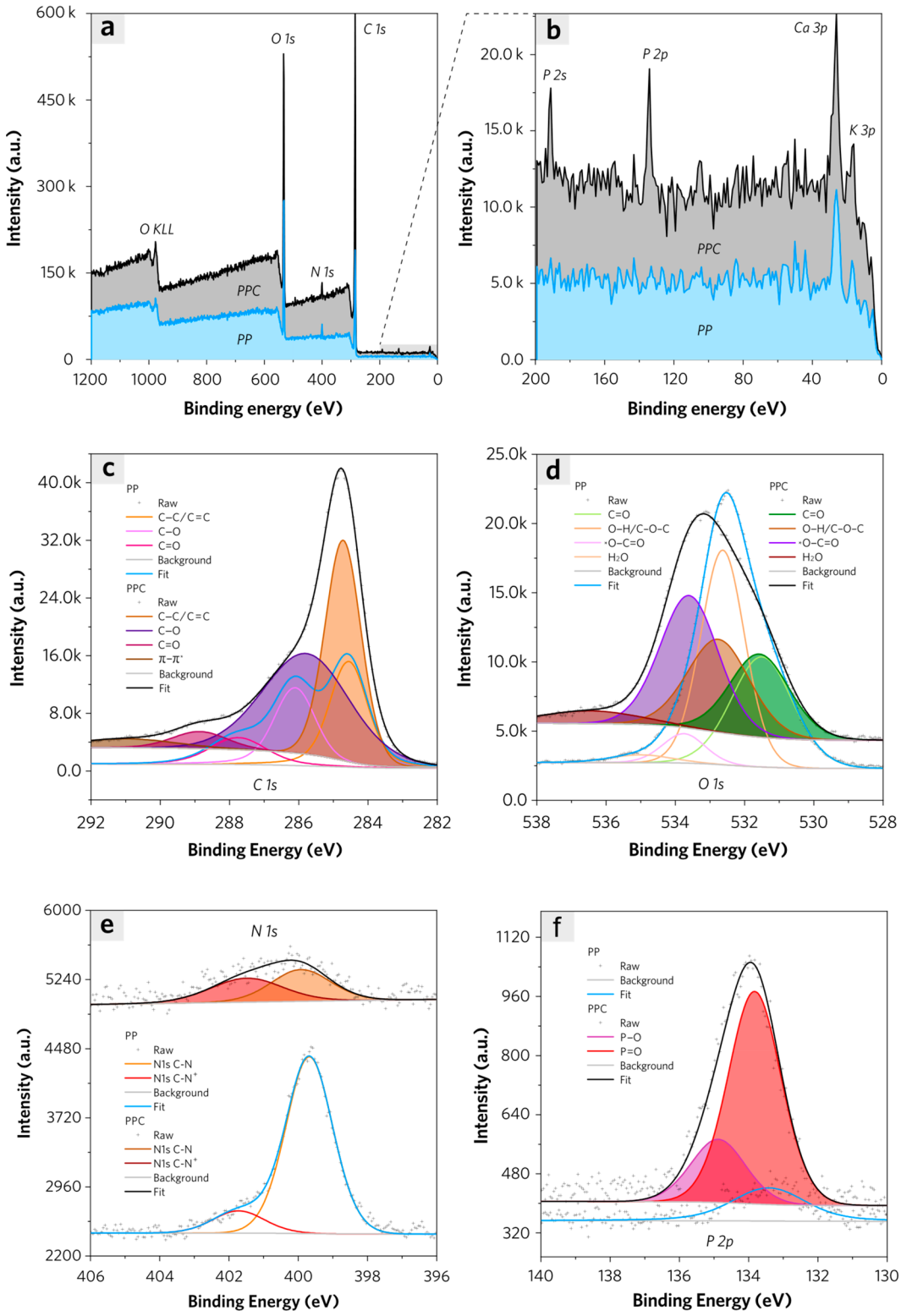

Figure 5. Wide-scan XPS patterns of PP and PPC (a) and the partially enlarged patterns (b). The high-resolution spectra of C-1s (c), O-1s (d), N-1s (e), and P-2p (f) for PP and PPC.

spectrum of PPC. In the case of the C-1s high-resolution spectrum (Figure 5c), it is deconvoluted into four peaks. The fitting peaks at 284.6 ± 0.2 eV are ascribed to both C−C and C=C bonds in both PP and PPC, which are hardly distinguished due to the overlap. The fitting peaks at 285.9 ± 0.2 eV are assigned to C−O bonds in alcohol and ether groups. The difference between the C=O features of PP (287.8 eV) and PPC (288.8 eV) is attributed to the chemical change from ester C=O to carboxylic acid C=O as depicted in their FTIR spectra. Moreover, the satellite peak at 291.0 eV corresponds to the C-1s shakeup effect owing to the $\pi-\pi^*$ transition of as-formed enhanced aromatic systems in PPC.[29]

https://doi.org/10.1021/acsomega.2c04799
ACS Omega 2022, 7, 46288−46302

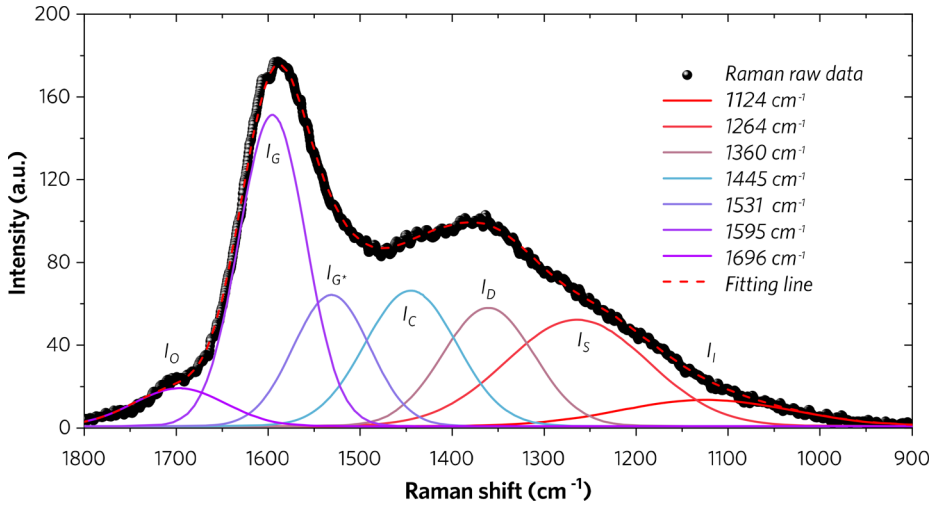

Figure 6. Raman spectrum of PPC and the corresponding deconvoluted bands with a 532 nm wavelength laser source.

The detailed fitting curves of the corresponding O-1s high-resolution spectra are exhibited in Figure 5d. Except for the peak ascribed to oxygen sites in free H_2O, the fitting peaks at around 531.5 eV (peak-1), 532.6 eV (peak-2), and 533.6 eV (peak-3) are successively assigned to oxygen sites in C=O, O−H/C−O−C, and O*−C=O groups. The integral area of peak-2 versus the total area of O-1s peak is significantly reduced, demonstrating the evidence of dehydration and carbonization in the synthesis of PPC from PP. According to Figure 5e, the N-1s high-resolution spectra of PP and PPC have also been deconvoluted into two peaks. The fitting peaks at 399.8 ± 0.1 eV are assigned to C−N, and the peaks at 401.6 ± 0.1 eV are assigned to R_4−N^+ (quaternary amine groups). As a result, the loss of nitrogen-containing compounds like alkaloids is significant in the synthesized PPC from PP. The quaternary amine groups are the main surface nitrogen-containing groups in PPC.

Phosphorus has been proven to be linked to PPC structure, but the bonding of phosphorus structure should be addressed. As for the P-2p deconvolution results, Claeyssens et al. consider that the fitting peak centered at 130.7 eV is assigned to P−P bonds in phosphorus carbides with no obvious evidence of the contribution of P−C bonds to this feature.[30] Liu et al. describe the fitting peak at 131.3 eV to P−P or P−H in the P-2p spectrum of phosphorus-doped tetrahedral amorphous carbon.[31] However, Yang et al. ascribe the fitting peak at a binding energy of 132.7 eV to P−C.[32] In any case, the raw peak at 134.1 eV is attributed to P sites bonded to O owing to its much higher binding energy as compared with the above-discussed situation.[33] Two fitting peaks at 133.9 eV ascribed to P−O and 134.9 eV corresponding to P=O are distinguished in the P-2p spectrum of PPC as shown in Figure 5f, which are consistent with its FTIR results. Therefore, phosphate ester with terminal hydroxyl groups, like C−O−P=O(OH)$_2$, is supposed to be the most probable bonded P structure in PPC.

3.4. Aromaticity Characterization of PPC. The Raman spectrum of PPC is conducted as shown in Figure 6, which can provide insight into the polarizable vibrations of C=C in aromatics and molecular backbones of carbon materials. According to the above FTIR analysis, PP-250 and PPC show a significant decrease in pristine functional groups as compared with PP. Two broad peaks at 1600−1580 cm^{-1} and 1380−1325 cm^{-1} can be observed in the Raman spectrum of PPC. The fundamental vibration of the E_{2g} stretching modes of all pairs of sp^2 carbon atoms in aromatic rings (G band) and symmetry breaking at the edges of graphite planes in sp^2 carbon (D band) have been well accepted in graphite Raman research. Unlike these carbon materials with highly ordered conjugated structures, PPC has a broad Raman spectrum because of the multiple overlapping peaks of the neighboring carbonaceous species associated with cellulose and lignin-derived carbon structures. It can be deconvoluted into several bands according to the reported band assignment methods.[34,35] The peak I_O at 1696 cm^{-1} is assigned to the carbonyl C=O structure which is consistent with the corresponding adsorption band in the IR spectrum. The peak I_G at 1595 cm^{-1} represents aromatic ring quadrant breathing rather than E_{2g} fundamental vibration for graphite in PPC with consideration of no convincing signs for the formation of graphitic crystallite structures in such a low-temperature pyrolysis process. Both peaks I_{G*} at 1531 cm^{-1} and I_C at 1445 cm^{-1} are attributed to aromatic semicircle ring stretch for aromatic ring systems with more than two fused benzene rings in the amorphous carbon structure. The peak I_D at 1360 cm^{-1} is ascribed to sp^2 carbon in aromatics with six or more fused benzene rings but less than that in graphite, which indicates the presence of medium-to-large-sized aromatic rings in PPC. Besides the above assigned five peaks, the peak I_S at 1264 cm^{-1} is attributed to the sp^3 carbon in aromatic structures, especially like alkyl-aryl ether and C−C on hydroaromatic rings in lignin-derived structure in PPC. The small peak I_I at 1124 cm^{-1} corresponds to C−H on aromatic rings.

3.5. Adsorption Kinetics. Three kinetic models are applied to mathematically describe the adsorption of each ionic dye.[36] The nonlinear forms of the pseudo-first-order (PFO) model and pseudo-second-order (PSO) model are presented as eq 1 and eq 2, respectively. The linear form of the intraparticle diffusion (IPD) model is presented in eq 3.

$$q_t = q_e - q_e \cdot e^{-k_1 \cdot t} \quad (1)$$

$$q_t = \frac{q_e^{\,2} K_2 t}{1 + q_e k_2 t} \quad (2)$$

https://doi.org/10.1021/acsomega.2c04799
ACS Omega 2022, 7, 46288−46302

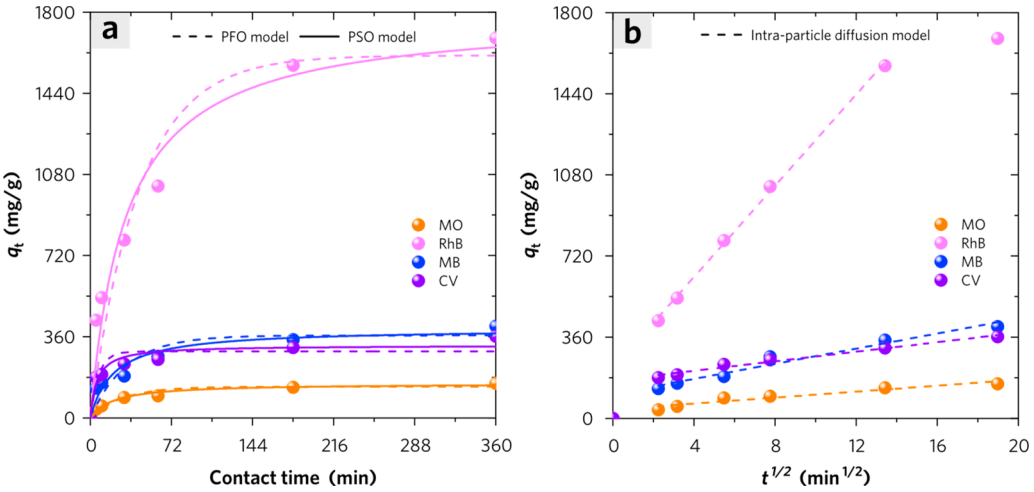

Figure 7. (a) The plots of PFO and PSO model simulation for kinetic curves of dye adsorption on PPC. (b) The plots of IPD model simulation for kinetic curves of dye adsorption on PPC. The adsorbent dosage is 0.5 g/L, and the adsorbed dyes are MO (c_0 = 200 ppm), RhB (c_0 = 1000 ppm), MB (c_0 = 300 ppm), and CV (c_0 = 300 ppm).

Table 2. Adsorption Kinetic Parameters Obtained from Nonlinear Model Equations Fitting Method[a]

kinetic model	temp	parameters	MO	RhB	MB	CV
pseudo-first-order	298 K	$q_{e,cal}$	138.3	1607.9	365.7	295.0
		k_1	0.0352	0.0229	0.0312	0.1362
		adj. R^2	0.9205	0.9220	0.8521	0.8447
pseudo-second-order	298 K	$q_{e,cal}$	152.9	1791.0	396.0	321.7
		k_2	0.000315	0.0000174	0.000122	0.000535
		adj. R^2	0.9733	0.9585	0.9206	0.9226
intraparticle diffusion	298 K	k_{ip}	6.608	101.263	16.763	10.578
		C	39.1	221.3	108.0	168.5
		adj. R^2	0.9024	0.9981	0.9541	0.9742
initial adsorption factor		R_i	0.7452	0.8688	0.7347	0.5351

[a]Except for the intraparticle diffusion model.

$$q_t = k_{ip}\sqrt{t} + C \quad (3)$$

where q_e (mg/g) and q_t (mg/g) are the amounts of adsorbate on PPC at equilibrium and at any time t (min); k_1 (min^{-1}), k_2 (g mg^{-1} min^{-1}), and k_{ip} (mg g^{-1} min$^{-0.5}$) are the adsorption rate constant of the PFO, PSO, and IPD model, respectively; C (mg/g) is a constant related to the thickness of the limiting boundary layer or initial adsorption behavior. Table 2 provides the corresponding kinetic parameters for each dye adsorption on PPC at 298 K.

As shown in Figure 7a,b, the IPD model fits the experimental data of MB, CV, and RhB adsorption with the highest adj. R^2 values (0.954−0.998), which are better than that of the PFO model (0.845−0.922) and PSO model (0.923−0.959). However, the experimental data of MO adsorption is fitted well by the PSO model with the highest adj. R^2 values of 0.973. In Figure 7b, the intraparticle diffusion plots show linear regions, not passing through the origin, which indicate the adsorption process is controlled by film diffusion during initial adsorption.[37] Due to the significant difference of the constant C for different dye adsorption, it exhibits great differences in initial adsorption quantities of cationic and anionic dyes at the very beginning of the adsorption procedure. In the forced stirring case, the film diffusion is negligible. The intraparticle diffusion becomes a rate-limiting step when considering the steric hindrance effect if the pore aperture is too narrow for adsorbate molecules to quickly diffuse into deeper sites.[38] The initial adsorption factors for the IPD model indicate the adsorption behaviors of these dyes on PPC belong to the "intermediately initial adsorption" type (Table S1), which indicates the possibility of rapid adsorption occurring at the beginning.[39] This rapid adsorption behavior can be likely driven by strong interactions between dye molecules and limited surface sites of PPC.

3.6. Adsorption Isotherms. To evaluate the adsorption performance of PPC, four different kinds of dyes were used for the isothermal adsorption experiments. These dyes are methyl orange (MO) as an anionic dye because of sulfonic anion, rhodamine B (RhB) as a neutral dye attributed to its intramolecular carboxylic anion and quaternary ammonium cation, methylene blue (MB) as a cationic dye because of the quaternary ammonium cation, and crystal violet (CV) as cationic dye owing to quaternary ammonium cation in its hydrochloride form. According to Figure 8a, PPC exhibits a much higher equilibrium adsorption capacity (q_e) of these dyes than PP. To be specific, PPC shows enhanced adsorption capacity of RhB with an increase of 1545%, MO with an increase of 840%, MB with an increase of 123%, and CV with an increase of 112%, when it is compared with PP. The equilibrium adsorption capacity of each dye (isotherm) shows a rapid rise at the low initial dye concentration; however, it tends to reach a plateau stage as the adsorbate equilibrium concentration rises eventually (Figure 8b). Three different

https://doi.org/10.1021/acsomega.2c04799
ACS Omega 2022, 7, 46288−46302

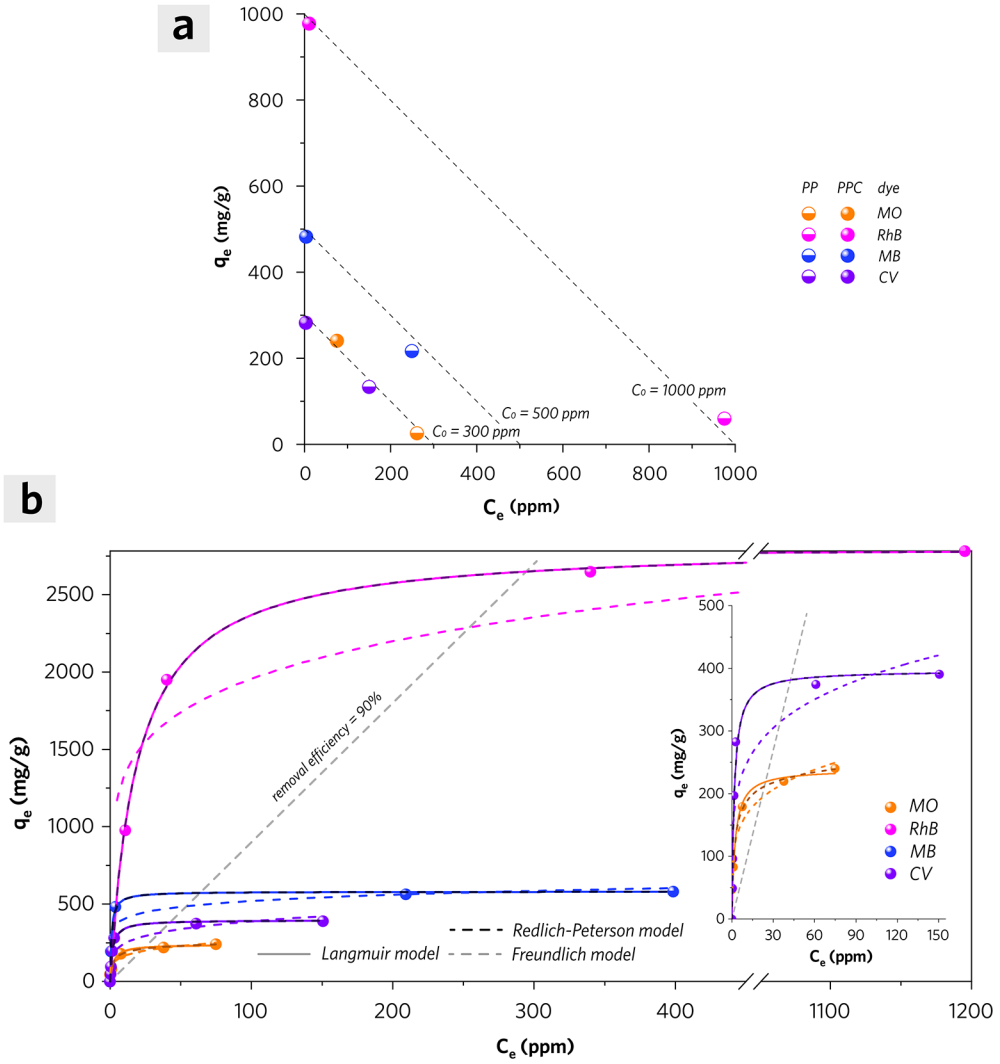

Figure 8. (a) The equilibrium adsorption capacity of each dye onto PP and PPC (adsorbent dosage of 1 g/L, MO with c_0 of 300 ppm, RhB with c_0 of 1000 ppm, MB with c_0 of 500 ppm, and CV with c_0 of 300 ppm at 298 K). (b) The adsorption isotherms for MO, RhB, MB, and CV adsorption on PPC (adsorbent dosage of 1 g/L) at 25 °C (298 K) and their fitting curves by Langmuir (solid line in color), Freundlich (dashed line in color), and Redlich−Peterson (dashed line in dark color) model.

Table 3. Adsorption Isotherm Parameters of Each Dye Adsorption on PPC by Langmuir, Freundlich, and Redlich−Peterson Models

isotherm model	corresponding value	MO	RhB	MB	CV
Langmuir	Q_{max}	239.1	2821.8	580.5	396.6
	K_L	0.444	0.0522	1.03	0.592
	adj. R^2	0.945	0.999	0.996	0.975
separation factor	R_L	0.011−0.082	0.005−0.019	0.001−0.005	0.005−0.063
Freundlich	K_F	102.3	899.8	316.5	154.4
	n	4.84	5.93	9.28	5.00
	adj. R^2	0.948	0.777	0.617	0.752
Redlich−Peterson	K_R	147.8	147.3	596.5	234.7
	a_R	0.820	0.0522	1.03	0.592
	β	0.93	1	1	1
	adj. R^2	0.931	0.999	0.994	0.968

adsorption models are used to describe the mechanisms of each dye adsorption system.

3.6.1. Langmuir Isotherm. Adsorbates are attracted by specific homogeneous sites within the adsorbent in monolayer adsorption according to the basic assumption of the Langmuir isotherm[15] presented as eq 4:

$$q_e = \frac{Q_{max} \cdot K_L \cdot c_e}{1 + K_L \cdot c_e} \quad (4)$$

where q_e is the equilibrium solid-phase concentration of adsorbates (mg/g); c_e is the equilibrium liquid-phase concentration of adsorbates (mg/L); Q_{max} and K_L are the

https://doi.org/10.1021/acsomega.2c04799
ACS Omega 2022, 7, 46288−46302

Langmuir parameters related to the theoretical maximum monolayer adsorption capacity and adsorption energy, respectively. The calculated Q_{max} values for MO, RhB, MB, and CV according to their Langmuir isotherms are 239.1, 2821.8, 580.5, and 396.6 mg/g, respectively. The Q_{max} of the anionic dye (MO) isotherm is much less than that of either cationic or neutral dyes.

The essential characteristics of the Langmuir monolayer adsorption process can be determined by the separation factor R_L, which is defined by eq 5:

$$R_L = \frac{1}{1 + K_L \cdot c_0} \quad (5)$$

The R_L values were found to vary, but all lie within a range from 0 to 1 as shown in Table 3. This indicates the favorable isotherm shape of the Langmuir model for each dye adsorption on PPC.

3.6.2. Freundlich Isotherm. Heterogeneous sites with a nonuniform distribution of adsorption energies within the adsorbent are prevailing according to the basic assumption of Freundlich isotherm[15] presented as eq 6:

$$q_e = K_F \cdot c_e^{1/n} \quad (6)$$

where q_e is the equilibrium solid-phase concentration of adsorbates (mg/g); c_e is the equilibrium liquid-phase concentration of adsorbates (mg/L); K_L and n are Freundlich isotherm parameters related to adsorption capacity and intensity, respectively. The n value for the MO isotherm is calculated as 4.84 (Henry region) with an adjusted R-square value of 0.948, which indicates a favorable isotherm shape ($1 < n < 10$). The RhB, MB, and CV isotherms are not applicable to this model due to their low adjusted R-squared values (Table 3).

3.6.3. Redlich–Peterson Isotherm. The Redlich–Peterson isotherm model employs three parameters in its formula to combine the Langmuir and Freundlich equations.[15] It can be applied to either inhomogeneous or heterogeneous adsorption systems as depicted in eq 7:

$$q_e = \frac{K_R \cdot c_e}{1 + a_R \cdot c_e^{\beta}} \quad (7)$$

where q_e is the equilibrium solid-phase concentration of adsorbates (mg/g); c_e is the equilibrium liquid-phase concentration of adsorbates (mg/L); K_R and a_R are Redlich–Peterson isotherm parameters; β is the exponent, which is within a range from 0 to 1. The β value for the MO isotherm is 0.93, suggesting that the adsorption of MO on PPC is appropriate for a heterogeneous adsorption system. However, the RhB, MB, and CV isotherms are more applicable to the Langmuir model due to their β value being close to 1 (Table 3). On the basis of the Redlich–Peterson model, the maximum initial concentration of each dye solution for acquiring 90% removal efficiency is estimated to be 234.55 ppm (MO), 2943.8 ppm (RhB), 633.8 ppm (MB), and 423.6 ppm (CV) at 298 K with an adsorbent dosage of 1 g/L.

3.6.4. Adsorption Thermodynamics. Thermodynamics is favorable for predicting adsorption mechanisms, and the standard change of Gibbs free energy in the adsorption process can be calculated as eq 8:

$$\Delta G^\circ = -RT \ln K_c \quad (8)$$

where R is the universal gas constant, T is the temperature in Kelvin, and K_c is a standard equilibrium constant. K_c can be obtained as a dimensionless parameter by multiplying K_L (Langmuir equilibrium constant) by the molecule weight of adsorbate (MO, 327.34 g/mol; RhB, 479.02 g/mol; MB, 373.90 g/mol; CV, 407.99 g/mol), 1000 mg/g, and then c° (1 mol/L) according to the literature.[40] The calculated ΔG° value for each dye adsorption process is listed in Table 4.

Table 4. Calculated Equilibrium Constants (Langmuir Model) and Gibbs Energy for Each Dye Adsorption on PPC

parameter	MO	RhB	MB	CV
K_c	145339.0	25004.8	385117	241530
T (K)	298	298	298	298
ΔG°(kJ/mol)	−29.45	−25.09	−31.86	−30.71

3.7. pH Dependency of Ionic Dye Adsorption. The influence of the initial pH value on the equilibrium adsorption capacity of each dye on PPC is investigated with overall consideration of the charge polarity of adsorbate and adsorbent. As shown in Figures S3–S6, the simulated molecular structure species of each dye vary at different pH conditions, which contributes to the charge polarity of dye molecular ions. Meanwhile, the zeta potentials versus pH for PPC were also measured to verify the charge polarity of adsorbents at different pH in a liquid–solid system. It exhibits a significant decrease from 22.5 mV to −29.0 mV in the PPC zeta potential curve with initial pH varying from 3.0 to 11.0, which determines that its isoelectric point is around 5.5. As depicted in Figure 9a, MO exhibits negative charge polarity (E_{zeta} = −13.8 mV) at a pristine pH value of 6.81 due to sulfonic anion. The equilibrium adsorption capacity of MO decreases from 214.4 mg/g (pH 5.1) to 89.9 mg/g (pH 11.1). PPC shows a positive charge (E_{zeta} = 5.06 mV) at pH 5.0, which is opposite to the charge polarity of MO. Enhanced MO adsorption by electrostatic attraction effect occurs below the isoelectric point of PPC, which is consistent with the suppressed adsorption by electrostatic repulsion effect above the neutral pH value. According to Figure 9b, the equilibrium adsorption capacity of MB on PPC increases from 448.3 mg/g (pH 5.0) to 588.5 mg/g (pH 11.0), in which the rise of the initial pH value contributes to the transformation of the electrostatic force from repulsion to attraction between MB and PPC. The equilibrium adsorption capacity of CV on PPC versus initial pH also exhibited a positive correlation due to their enhanced electrostatic attractive force (Figure 9d), excluding its unfavorable adsorption behavior at pH 9.0 which is possibly due to the decreased solubility of CV in an alkaline aqueous system. The equilibrium adsorption capacity of RhB on PPC exhibits an M-shaped curve as the initial pH value increases from 2.9 to 11.0, in which the minimum adsorption capacity is 1478.0 mg/g with an initial pH value of 5.1 (Figure 9c). Either higher initial pH (pH 9.2) or lower initial pH (pH 2.9) is conducive to favorable adsorption of RhB on PPC.

3.8. Adsorption Mechanism. It has been commonly accepted that the mechanism for dye adsorption on activated carbon/biochar is mainly influenced by some critical factors: (1) adsorbent characteristics (specific surface area, pore structure, aromaticity, and surface chemistry); (2) adsorbate characteristics (molecular structure, solubility, initial concentration polarity, dissociation property, pK_a); (3) aqueous

https://doi.org/10.1021/acsomega.2c04799
ACS Omega 2022, 7, 46288−46302

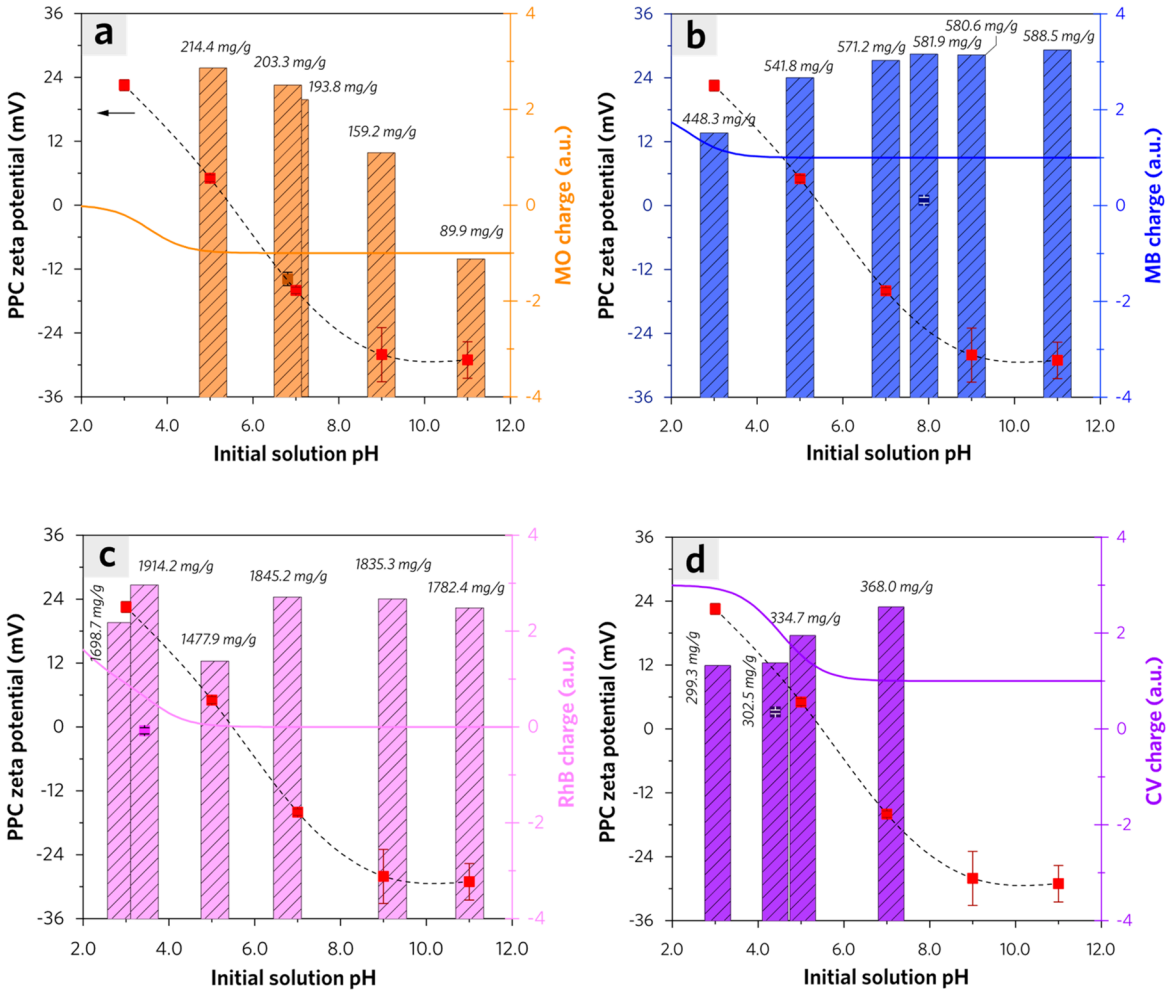

Figure 9. The equilibrium adsorption capacity data of each dye (0.5 g/L adsorbent dosage): (a) MO, c_0 = 182 ppm; (b) MB, c_0 = 592 ppm; (c) RhB, c_0 = 1417 ppm; (d) CV, c_0 = 379 ppm at different initial pH values (3.0, 5.0, 7.0, 9.0, 11.0, and their pristine pH), which are accompanied by the surface zeta potentials of PPC (adsorbent) under specific initial pH values (red square linked with dashed line), the surface zeta potential of each dye (adsorbate) under its pristine solution pH value (colored square in dark color), and the theoretical simulated charge value of each dye (adsorbate) in aqueous solution versus pH (colored solid line).

solution conditions (pH, temperature, interference factors). The classical adsorption mechanisms of organic pollutants bonding to biochar indicates adsorption is commonly driven by several adsorbent−adsorbate affinity forces, such as covalent bonding, electrostatic force (Coulombic force), H-bonding, π-interactions, dipole interactions, and hydrophobic forces.[41]

It is evident that there exist abundant micropores (56.4% of total pore volume) and mesopores (43.6% of total pore volume) in PPC, leading to its high surface area (877.3 m^2/g) and total pore volume (0.486 cm^3/g). The pore-filling effect contributes to the adsorption of dyes in pores as the size of the adsorbate molecule is comparable to the volume of pores.[42] According to the characterization, the heterogeneous surface functional groups like oxygenic groups (hydroxyl, carbonyl, carboxyl, and phosphate ester groups) and amine groups are linked to the low graphitized carbon frame structure of PPC. The FTIR spectra of the end product from dye-adsorbed PPC are shown in Figures S7−S10; the functional groups of organic dyes are probably favorable to interact with PPC by generating H-bonding, n−π and π−π interactions, which are also based on oxygenic groups, amine groups, and conjugated heterocyclic aromatic structures of dye molecules.[43] Electrostatic forces including attraction and repulsion should be also involved in adsorption mechanisms due to the significant pH dependency of the adsorption capacity of ionic dyes onto PPC. A detailed discussion of the adsorption synergetic mechanisms of ionic dyes on PPC follows.

3.8.1. Anionic Dye (MO) Adsorption on PPC. As depicted in Figure S3, the species distribution curve has revealed that MO can be mainly in molecular form IV within a wide pH range (5−14), in which the sulfonic anion determines its negative charges. As shown in Figure 10a, in weakly acidic (pH 5.0) systems, PPC exhibits positive charge polarity which is opposite to that of MO. Protonated nitrogenous groups in PPC contribute to active adsorption sites to MO driven by an electrostatic attractive force. In the weakly alkaline (pH 9.0) system, PPC exhibits negative charge polarity due to its deprotonated phosphate groups and carboxylate groups. It is evident that the electrostatic repulsive force between MO (adsorbate) and PPC (adsorbent) is unfavorable to the adsorption of MO, but the nonelectrostatic force is also non-negligible due to its considerable adsorption capacity of MO, which is 89.9 mg/g at pH 11.0. In detail, pore filling (Table S2) and π interactions (Figure S7) are probably the main propelling effects for the adsorption of MO in alkaline conditions.

https://doi.org/10.1021/acsomega.2c04799
ACS Omega 2022, 7, 46288−46302

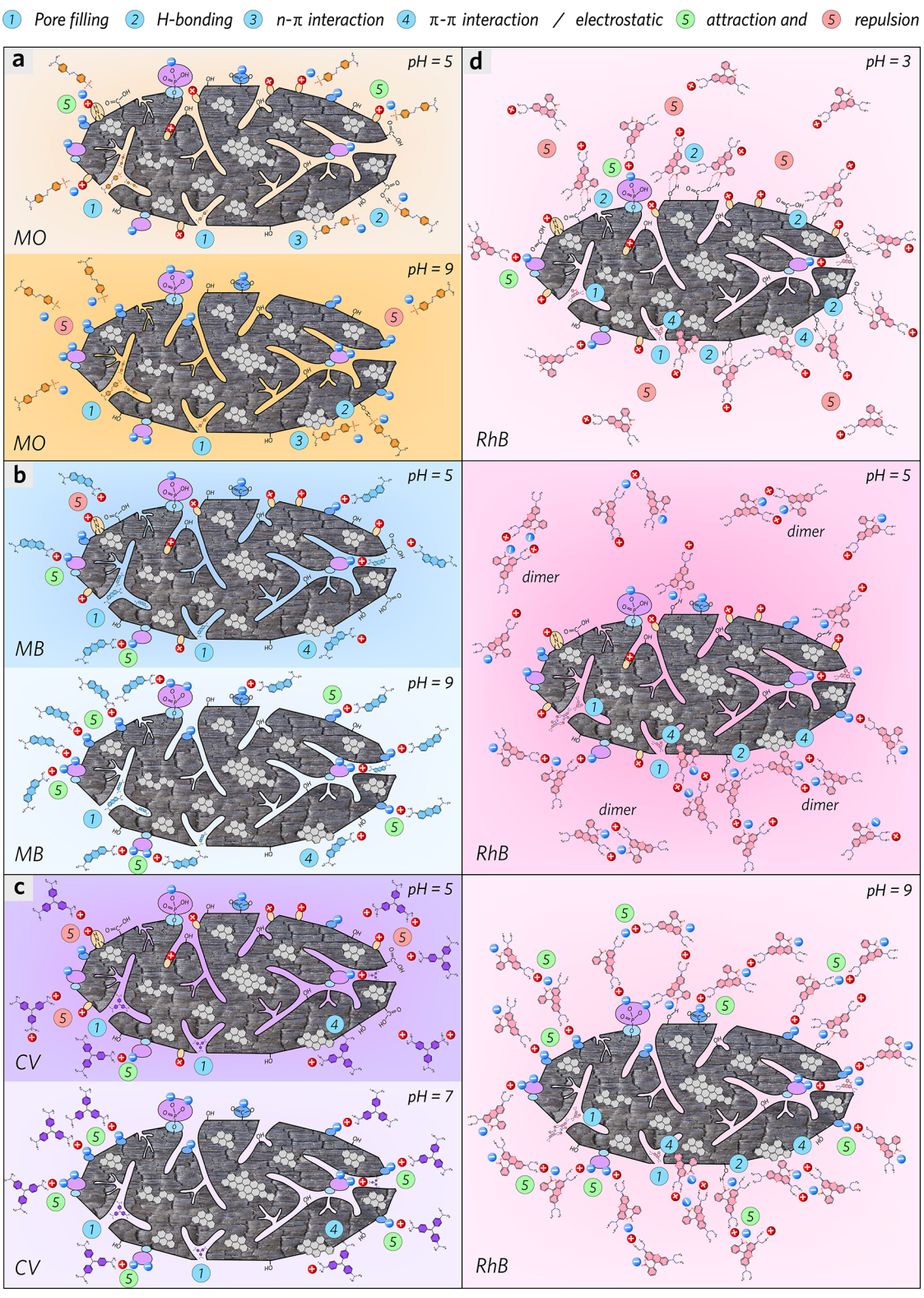

Figure 10. Probable intermolecular forces driving adsorption of (a) MO, (b) MB, (c) CV, and (d) RhB on PPC at different initial pH values.

3.8.2. Cationic Dye (MB and CV) Adsorption on PPC. MB and CV can be considered stable cationic dyes with quaternary ammonium (which exists in molecular form III as shown in Figures S4 and S5) within a wide pH range (3−11), whereas the solubility of CV decreases in aqueous solution under alkaline conditions. Due to the electrostatic force transition from repulsion to the attraction between adsorbate (cationic dye) and adsorbent (PPC), the adsorption capacity of either MB or CV increases as the initial pH rises from 3.0 to 11.0. On the other hand, the adsorption capacity of either MB or CV remains at a high level at pH 3.0, which indicates the contribution of the nonelectrostatic force primarily dominates in the adsorption process. Except for the pore filling (Table S2), the n−π and π−π interactions (Figures S8 and S9) are

https://doi.org/10.1021/acsomega.2c04799
ACS Omega 2022, 7, 46288−46302

possibly the main propelling effect due to the high aromaticity of PPC and dye molecules.[44]

3.8.3. Neutral Dye (RhB) Adsorption on PPC. RhB has shown a more complicated charge polarity property due to the pK_a difference between its intramolecular carboxylic group and quaternary ammonium. RhB exhibits positive charge polarity within a pH value below 3.0, which is attributed to quaternary ammonium in its molecular form III, protonated quaternary ammonium in form II, and oxonium ylide in form I (Figure S6). It has shown a neutral molecular form IV within a pH value above 5.0 because there exists an existing quaternary ammonium cation and a carboxylate anion in each RhB molecule. This demonstrates that the pore-filling effect and nonelectrostatic forces are favorable to the adsorption process all through the pH range when considering the minimum adsorption remains as high as 1478.0 mg/g at pH 5.1 (Table S2 and Figure S10). The self-aggregation of RhB molecules due to the electrostatic interactions between the carboxyl and xanthene groups is favorable to form the zwitterionic molecules (dimer) at a solution pH above 3.5. At the isoelectric point of PPC (being close to pH 5.1), the RhB aggregations are less favorable to adsorption on PPC with net zero surface charge.[45] When the initial solution pH comes to 3.4, the adsorption capacity of RhB increases to 1914.2 mg/g, which is probably attributed to the enhanced H-bonding interaction between carboxylic acid groups of RhB and oxygenic groups of PPC (Figure S10). When the initial solution pH comes to 2.9, the enhanced electrostatic repulsive force leads to a slight decrease in RhB adsorption capacity. PPC shows favorable adsorption of RhB when pH is above 7.0 due to the pore-filling effect, electrostatic attractive forces, and π interactions.

4. CONCLUSIONS

In this work, PPC was produced from pomelo peel, undergoing chemical activation and pyrolysis at a relatively low temperature of 250 °C in a non-circulated air atmosphere. Phosphoric acid has played a key role in the formation of the cross-linked carbonaceous precursor (PP-250), which is critical for the purpose of acquiring high porosity and aromaticity for PPC during thermal treatment. The possible active sites, which are favorable for the adsorption of ionic dyes on PPC, are surface oxygenic groups, including hydroxyl groups, carboxylate groups (negative charge source), phosphate ester (negative charge source), and quaternary ammonium (positive charge source). PPC exhibits high adsorption capacity of RhB (2821.8 mg/g), MB (580.5 mg/g), CV (396.6 mg/g), and MO (239.1 mg/g), which is obtained by the Langmuir model. The intraparticle diffusion may influence the adsorption kinetic process of ionic dyes on PPC. The probable adsorption mechanism has been discussed based on the factors in their adsorption systems. In brief, the major conclusions can be given as follows:

(1) Nonelectrostatic forces, especially n−π and π−π interactions, contribute to the adsorption of dyes with aromatic structures based on fused benzene or conjugated heterocyclic rings on PPC.

(2) The electrostatic force is the major reason for the pH-dependency character in the adsorption of ionic dyes with single-polarity charges, such as MO, MB, and CV. For RhB, those factors, including electrostatic force, self-aggregation, and H-bonding, generate a synergetic effect on its pH-dependent adsorption behavior.

(3) PPC shows favorable adsorption of cationic dye, including MB and CV, under alkaline conditions. On the other hand, it shows enhanced adsorption of an anionic dye like MO under acidic conditions.

■ ASSOCIATED CONTENT

Supporting Information

The Supporting Information is available free of charge at https://pubs.acs.org/doi/10.1021/acsomega.2c04799.

Schematic diagram of PPC preparation method, UV−vis absorption spectrum of diluted dye solution at different initial pH conditions, simulated molecular ionic structures of dyes at different pH conditions, FTIR spectra of dye-adsorbed PPC compared to that of either PPC or dye, explanation of initial adsorption factor according to IPD model, and comparison of adsorption performance of synthesized biochar reported in past works in the literature (PDF)

■ AUTHOR INFORMATION

Corresponding Author

Qiang Zhao − *College of Science, Civil Aviation University of China (CAUC), Tianjin 300300, China;* orcid.org/0000-0002-2545-2383; Email: zhao-q@cauc.edu.cn

Authors

Fang Wei − *College of Science, Civil Aviation University of China (CAUC), Tianjin 300300, China;* orcid.org/0000-0003-4462-0562

Yuwei Zhu − *College of Science, Civil Aviation University of China (CAUC), Tianjin 300300, China*

Tongmin He − *College of Science, Civil Aviation University of China (CAUC), Tianjin 300300, China*

Shengpu Zhu − *College of Science, Civil Aviation University of China (CAUC), Tianjin 300300, China*

Tianhao Wang − *College of Science, Civil Aviation University of China (CAUC), Tianjin 300300, China*

Chunyi Yao − *College of Science, Civil Aviation University of China (CAUC), Tianjin 300300, China*

Chenlu Yu − *College of Science, Civil Aviation University of China (CAUC), Tianjin 300300, China*

Peipei Huang − *School of Physics & Information Technology, Shaanxi Normal University, Xi'an 710119, China*

Yan Li − *College of Science, Civil Aviation University of China (CAUC), Tianjin 300300, China*

Weiguo Song − *Laboratory of Molecular Nanostructure and Nanotechnology, Institute of Chemistry, Chinese Academy of Sciences, Beijing 100190, China;* orcid.org/0000-0001-5390-6787

Complete contact information is available at: https://pubs.acs.org/10.1021/acsomega.2c04799

Notes

The authors declare no competing financial interest.

■ ACKNOWLEDGMENTS

This work was financially supported by the Fundamental Research Funds for the Central Universities (Project No. 3122019153) and the Scientific Research Initial Funding of Civil Aviation University of China (Project No. 2020KYQD95).

REFERENCES

(1) Mirnasab, M.; Hashemi, H.; Samaei, M.; Azhdarpoor, A. Advanced removal of water NOM by Pre-ozonation, Enhanced coagulation and Bio-augmented Granular Activated Carbon. *Int. J. Environ. Sci. Technol.* **2021**, *18* (10), 3143−3152.

(2) Ismail, M.; Akhtar, K.; Khan, M.; Kamal, T.; Khan, M. A.; M Asiri, A.; Seo, J.; Khan, S. B. Pollution, toxicity and carcinogenicity of organic dyes and their catalytic bio-remediation. *Curr. Pharm. Des.* **2019**, *25* (34), 3645−3663.

(3) Parvaresh, V.; Hashemi, H.; Khodabakhshi, A.; Sedehi, M. Removal of dye from synthetic textile wastewater using agricultural wastes and determination of adsorption isotherm. *Desalin. Water Treat.* **2018**, *111*, 345−350.

(4) Nasiri, A.; Rajabi, S.; Hashemi, M. CoFe2O4@ Methylcellulose/AC as a New, Green, and Eco-friendly Nano-magnetic adsorbent for removal of Reactive Red 198 from aqueous solution. *Arabian J. Chem.* **2022**, *15* (5), 103745.

(5) Zhao, Q.; Zhang, C.; Tong, X.; Zou, Y.; Li, Y.; Wei, F. Fe3O4-NPs/orange peel composite as magnetic heterogeneous Fenton-like catalyst towards high-efficiency degradation of methyl orange. *Water Sci. Technol.* **2021**, *84* (1), 159−171.

(6) Ahsan, M. A.; Jabbari, V.; El-Gendy, A. A.; Curry, M. L.; Noveron, J. C. Ultrafast catalytic reduction of environmental pollutants in water via MOF-derived magnetic Ni and Cu nanoparticles encapsulated in porous carbon. *Appl. Surf. Sci.* **2019**, *497*, 143608.

(7) Chan, S. H. S.; Yeong Wu, T.; Juan, J. C.; Teh, C. Y. Recent developments of metal oxide semiconductors as photocatalysts in advanced oxidation processes (AOPs) for treatment of dye wastewater. *J. Chem. Technol. Biotechnol.* **2011**, *86* (9), 1130−1158.

(8) Wu, S.; Hu, Y. H. A comprehensive review on catalysts for electrocatalytic and photoelectrocatalytic degradation of antibiotics. *Chem. Eng. J.* **2021**, *409*, 127739.

(9) Fonseca Couto, C.; Lange, L. C.; Santos Amaral, M. C. A critical review on membrane separation processes applied to remove pharmaceutically active compounds from water and wastewater. *J. Water Process Eng.* **2018**, *26*, 156−175.

(10) Zhou, L.; Huang, J.; He, B.; Zhang, F.; Li, H. Peach gum for efficient removal of methylene blue and methyl violet dyes from aqueous solution. *Carbohydr. Polym.* **2014**, *101*, 574−581.

(11) Li, C.; Wang, X.; Meng, D.; Zhou, L. Facile synthesis of low-cost magnetic biosorbent from peach gum polysaccharide for selective and efficient removal of cationic dyes. *Int. J. Biol. Macromol.* **2018**, *107*, 1871−1878.

(12) Zhou, L.; Xu, Z. Ultralight, highly compressible, hydrophobic and anisotropic lamellar carbon aerogels from graphene/polyvinyl alcohol/cellulose nanofiber aerogel as oil removing absorbents. *J. Hazard. Mater.* **2020**, *388*, 121804.

(13) Zeng, S.; Long, J.; Sun, J.; Wang, G.; Zhou, L. A review on peach gum polysaccharide: Hydrolysis, structure, properties and applications. *Carbohydr. Polym.* **2022**, *279*, 119015.

(14) Oliveira, J. M.; e Silva, M. R. d. L.; Issa, C. G.; Corbi, J. J.; Damianovic, M. H.; Foresti, E. Intermittent aeration strategy for azo dye biodegradation: A suitable alternative to conventional biological treatments? *J. Hazard. Mater.* **2020**, *385*, 121558.

(15) Günay, A.; Arslankaya, E.; Tosun, I. Lead removal from aqueous solution by natural and pretreated clinoptilolite: adsorption equilibrium and kinetics. *J. Hazard. Mater.* **2007**, *146* (1−2), 362−371.

(16) Anstey, A.; Vivekanandhan, S.; Rodriguez-Uribe, A.; Misra, M.; Mohanty, A. K. Oxidative acid treatment and characterization of new biocarbon from sustainable Miscanthus biomass. *Sci. Total Environ.* **2016**, *550*, 241−247.

(17) Perrich, J. R.*Activated Carbon Adsorption for Wastewater Treatment*; CRC Press, 2018.

(18) Sewu, D. D.; Boakye, P.; Woo, S. H. Highly efficient adsorption of cationic dye by biochar produced with Korean cabbage waste. *Bioresour. Technol.* **2017**, *224*, 206−213.

(19) Liang, Q.; Liu, Y.; Chen, M.; Ma, L.; Yang, B.; Li, L.; Liu, Q. Optimized preparation of activated carbon from coconut shell and municipal sludge. *Mater. Chem. Phys.* **2020**, *241*, 122327.

(20) Mohan, D.; Sarswat, A.; Ok, Y. S.; Pittman, C. U., Jr Organic and inorganic contaminants removal from water with biochar, a renewable, low cost and sustainable adsorbent-a critical review. *Bioresour. Technol.* **2014**, *160*, 191−202.

(21) Ren, Y. M.; Cui, C.; Wang, P. J. Pomelo Peel Modified with Citrate as a Sustainable Adsorbent for Removal of Methylene Blue from Aqueous Solution. *Molecules* **2018**, *23* (6), 1342.

(22) Zhao, T.; Yao, Y.; Li, D. R.; Wu, F.; Zhang, C. Z.; Gao, B. Facile low-temperature one-step synthesis of pomelo peel biochar under air atmosphere and its adsorption behaviors for Ag(I) and Pb(II). *Sci. Total Environ.* **2018**, *640*, 73−79.

(23) Zhang, B.; Wu, Y.; Cha, L. Removal of methyl orange dye using activated biochar derived from pomelo peel wastes: performance, isotherm, and kinetic studies. *J. Dispersion Sci. Technol.* **2020**, *41* (1), 125−136.

(24) Wu, Y.; Cha, L.; Fan, Y.; Fang, P.; Ming, Z.; Sha, H. Activated biochar prepared by pomelo peel using H3PO4 for the adsorption of hexavalent chromium: performance and mechanism. *Water, Air, Soil Pollut.* **2017**, *228* (10), 405.

(25) Renier, M. L.; Kohn, D. H. Development and characterization of a biodegradable polyphosphate. *J. Biomed. Mater. Res.* **1997**, *34* (1), 95−104.

(26) Guo, Y.; Rockstraw, D. A. Activated carbons prepared from rice hull by one-step phosphoric acid activation. *Microporous Mesoporous Mater.* **2007**, *100* (1−3), 12−19.

(27) Puziy, A.; Poddubnaya, O.; Martınez-Alonso, A.; Suárez-Garcıa, F.; Tascón, J. Synthetic carbons activated with phosphoric acid: I. Surface chemistry and ion binding properties. *Carbon* **2002**, *40* (9), 1493−1505.

(28) Bellamy, L.*The infra-red spectra of complex molecules*; Springer Science & Business Media, 2013.

(29) Tran, H. N.; Tomul, F.; Ha, N. T. H.; Nguyen, D. T.; Lima, E. C.; Le, G. T.; Chang, C.-T.; Masindi, V.; Woo, S. H. Innovative spherical biochar for pharmaceutical removal from water: Insight into adsorption mechanism. *J. Hazard. Mater.* **2020**, *394*, 122255.

(30) Claeyssens, F.; Fuge, G.; Allan, N.; May, P.; Ashfold, M. Phosphorus carbides: theory and experiment. *Dalton Trans.* **2004**, No. 19, 3085−3092.

(31) Han, J.; Liu, A.; Zhu, J.; Tan, M.; Wu, H. Effect of phosphorus content on structural properties of phosphorus incorporated tetrahedral amorphous carbon films. *Appl. Phys. A: Mater. Sci. Process.* **2007**, *88* (2), 341−345.

(32) Yang, D.-S.; Bhattacharjya, D.; Inamdar, S.; Park, J.; Yu, J.-S. Phosphorus-doped ordered mesoporous carbons with different lengths as efficient metal-free electrocatalysts for oxygen reduction reaction in alkaline media. *J. Am. Chem. Soc.* **2012**, *134* (39), 16127−16130.

(33) Zhao, L.; Cao, X.; Zheng, W.; Scott, J. W.; Sharma, B. K.; Chen, X. Copyrolysis of biomass with phosphate fertilizers to improve biochar carbon retention, slow nutrient release, and stabilize heavy metals in soil. *ACS Sustainable Chem. Eng.* **2016**, *4* (3), 1630−1636.

(34) Li, X.; Hayashi, J.-i.; Li, C.-Z. FT-Raman spectroscopic study of the evolution of char structure during the pyrolysis of a Victorian brown coal. *Fuel* **2006**, *85* (12−13), 1700−1707.

(35) Kim, P.; Johnson, A.; Edmunds, C. W.; Radosevich, M.; Vogt, F.; Rials, T. G.; Labbé, N. Surface functionality and carbon structures in lignocellulosic-derived biochars produced by fast pyrolysis. *Energy Fuels* **2011**, *25* (10), 4693−4703.

(36) Qiu, H.; Lv, L.; Pan, B.-c.; Zhang, Q.-j.; Zhang, W.-m.; Zhang, Q.-x. Critical review in adsorption kinetic models. *J. Zhejiang Univ. Sci. A* **2009**, *10* (5), 716−724.

(37) Tran, H. N.; You, S. J.; Hosseini-Bandegharaei, A.; Chao, H. P. Mistakes and inconsistencies regarding adsorption of contaminants from aqueous solutions: A critical review. *Water Res.* **2017**, *120*, 88−116.

https://doi.org/10.1021/acsomega.2c04799
ACS Omega 2022, 7, 46288−46302

(38) Cheung, W.; Szeto, Y.; McKay, G. Intraparticle diffusion processes during acid dye adsorption onto chitosan. *Bioresour. Technol.* **2007**, *98* (15), 2897−2904.
(39) Wu, F.-C.; Tseng, R.-L.; Juang, R.-S. Initial behavior of intraparticle diffusion model used in the description of adsorption kinetics. *Chem. Eng. J.* **2009**, *153* (1−3), 1−8.
(40) Zhou, X.; Zhou, X. The unit problem in the thermodynamic calculation of adsorption using the Langmuir equation. *Chem. Eng. Commun.* **2014**, *201* (11), 1459−1467.
(41) Tong, Y.; McNamara, P. J.; Mayer, B. K. Adsorption of organic micropollutants onto biochar: a review of relevant kinetics, mechanisms and equilibrium. *Environ. Sci.: Water Res. Technol.* **2019**, *5* (5), 821−838.
(42) Dąbrowski, A. Adsorption—from theory to practice. *Adv. Colloid Interface Sci.* **2001**, *93* (1−3), 135−224.
(43) Tran, H. N.; Wang, Y.-F.; You, S.-J.; Chao, H.-P. Insights into the mechanism of cationic dye adsorption on activated charcoal: the importance of π-π interactions. *Process Saf. Environ. Prot.* **2017**, *107*, 168−180.
(44) Tran, H. N.; You, S.-J.; Chao, H.-P. Fast and efficient adsorption of methylene green 5 on activated carbon prepared from new chemical activation method. *J. Environ. Manage.* **2017**, *188*, 322−336.
(45) Anandkumar, J.; Mandal, B. Adsorption of chromium (VI) and Rhodamine B by surface modified tannery waste: Kinetic, mechanistic and thermodynamic studies. *J. Hazard. Mater.* **2011**, *186* (2−3), 1088−1096.

https://doi.org/10.1021/acsomega.2c04799
ACS Omega 2022, 7, 46288−46302